
Article:
Edwards, S.M., Harding, A.L., Leedale, J.A. et al. (2026) Translating in vitro buccal permeation to in vivo and whole-body exposure using in silico cell-based and physiologically-based pharmacokinetic modelling. International Journal of Pharmaceutics. 126701. ISSN: 0378-5173

https://doi.org/10.1016/j.ijpharm.2026.126701

Translating *in vitro* buccal permeation to *in vivo* and whole-body exposure using *in silico* cell-based and physiologically-based pharmacokinetic modelling

Sean M. Edwards[a,§], Amy L. Harding[b, ¶, §,1], Joseph A. Leedale[c], Steven D. Webb[c], Helen E. Colley[b,1], Robert A. Byers[d], Rachel N. Bearon[e] and Craig Murdoch[b]

[a]Department of Mechanical and Aerospace Engineering, University of Liverpool, Liverpool, UK

[b]School of Clinical Dentistry, Faculty of Health, University of Sheffield, Sheffield, UK

[c]Syngenta, Jeallott's Hill International Research Centre, Bracknell, UK

[d]Sheffield Dermatology Research, Faculty of Health, University of Sheffield, Sheffield, UK

[e]Department of Mathematics, King's College London, London, UK

[1]Corresponding authors: Helen E. Colley, School of Clinical Dentistry, Faculty of Health, University of Sheffield, Sheffield, S10 2TA, UK and Amy L. Harding, Liverpool Head and Neck Centre, Molecular and Clinical Cancer Medicine, University of Liverpool, Liverpool, L69 7BE, UK

[§]Authors contributed equally to this work.

¶ Current address: Liverpool Head and Neck Centre, Molecular and Clinical Cancer Medicine, University of Liverpool, Liverpool, L69 7BE, UK

Colour Figures: 6

Keywords: Mathematical modelling; Drug delivery; Oral mucosa; Toxicology; Permeation; Systems pharmacology; Chemical toxicity, PBPK

Highlights

- *In vitro-informed in silico modelling of buccal mucosa chemical permeation*
- *Cell-based in silico model that translates in vitro data to in vivo predictions*
- *The in silico model is histology-informed specific for the human buccal mucosa*
- *In vitro informed passive diffusion and permeability coefficients*
- *In silico model linked to PBPK modelling for whole-body chemical distribution*

Abstract

There is increasing interest in the delivery of chemicals to or through the oral buccal mucosa to avoid first-pass metabolism by the liver or the use of needles, which are associated with oral or parenteral administration. Moreover, buccal mucosa is several times more permeable than skin, making it an attractive route for controlled drug delivery via mucoadhesive films, tablets, and patches. Developing *in silico* models to predict rates of chemical permeation would greatly expediate experimental discovery to clinical use. However, predicting chemical permeation through the buccal mucosa is challenging due to limited availability of *ex vivo* human tissue for experimentation. Previously, we used tissue engineered buccal mucosa to parameterise an *in silico* model of buccal chemical permeation using partial differential equations, fitted to *in vitro* generated chemical permeation data of chemicals with known physiochemical properties. Here, we describe a new approach to predict *in vivo* permeation from *in vitro* data. The importance of the permeability barrier is included explicitly in the *in silico* models by parameterising from *in vitro* permeation experiments on buccal epithelium with fully formed or deficient permeability barriers. *In vivo* predictions are made by mapping mechanistic parameters, fitted to *in vitro* data, to *in vivo* cell geometry including cell layer thicknesses, cell-sizes and extracellular space. The predictions are tied to a physiologically-based pharmacokinetic model for whole-body chemical distribution that is validated against *in vivo* data. This combined *in vitro-in silico* approach has the potential to reduce animal experimentation and improve *in vivo* predictions for human buccal mucosa.

1. Introduction

Drug delivery via the gastrointestinal tract remains the dominant route for administration of many medicinals. However, when delivered this way, such bioactive chemicals are susceptible to gastrointestinal enzymatic degradation and extensive first-pass metabolism in the liver that limit their bioavailability. Parenteral administration circumvents these issues but introduces problems with compliance, particularly with the young, those with trypanophobia (fear of needles), and often requires clinical supervision to dispense medication. Transdermal delivery is a possibility but is challenging for most medicinals because of the low permeability of the skin. Not only is the skin's epidermis highly keratinised (*stratum corneum*), but it contains a significant permeability barrier in the upper granular layers of the *stratum spinosum*, just below the *stratum corneum*. Here, secreted ceramides, fatty acids and cholesterol are organised into lipid-rich lamellae and gel-phase that fill the intercellular spaces around corneocytes, producing a highly hydrophobic layer that is largely impermeable to all but lipophilic chemicals [1]. Epidermal permeability is further regulated by tight junctions present on the plasma membrane of keratinocytes in the *stratum spinosum*. Tight junctions are comprised of a complex of proteins that include claudins, occludin, junctional adhesion molecules (JAM) and zona occludins (ZO), which act by pulling adjacent cells tightly together, forming a gate that regulates the passage of molecules to the deeper layers of the epidermis and into the dermis [2].

The difficulties associated with skin-mediated drug delivery has led to advances in smart-material devices such as mucoadhesive tablets, cast films or electrospun membranes for topical administration directly to or through the oral mucosa (tissues lining the mouth), particularly the buccal (cheek) or sublingual (under the tongue) mucosa [3-7]. The attraction for delivering medicinals via the oral mucosa rather than skin is the difference in permeability between these two types of epithelia, with the oral mucosa possessing permeability that is several times greater than the skin [8]. This is because the buccal/sublingual epithelium is non-keratinised (devoid of a *stratum corneum*) and contains very few lamellae and membrane-coating granules [9], meaning that its lipid-rich permeability barrier is markedly reduced compared to skin [1], allowing many chemicals to readily permeate this type of epithelium. The delivery of several chemicals and even small peptides has been reported by these mucosal devices but as of yet, only a few (e.g., ondansetron, buprenorphine, naloxone, fentanyl, nicotine) are available on the market [4, 10].

Depending on their physiochemical properties (such as lipophilicity, charge, molecular weight and geometry etc) chemicals traverse the oral non-keratinised epithelium either across (transcellular) or between (paracellular) oral keratinocytes. Generally, small lipophilic chemicals favour the transcellular permeation route as they can dissolve in the amphiphilic

plasma membranes of keratinocytes and in the lipid-rich lamellae. The low levels of lipids within the outer *stratum spinosum* layers of buccal/sublingual epithelium mean that tight junctions are the principal determinants regulating the permeation of more hydrophilic molecules through the paracellular space in this tissue [11].

Due to technological advancements in drug delivery, it is projected that the number of chemicals delivered via the buccal/sublingual mucosa will dramatically increase [6]. In addition, there is also a need to assess the toxicity profiles of other agents, such as agrochemicals and oral health products that come into contact with the oral mucosa. Laboratory-based methods to measure chemical permeation include the use of porcine buccal mucosa or tissue engineered *in vitro* human buccal mucosa that are time consuming and would need to be performed for every chemical screened. An alternative approach is to pre-screen using *in silico* modelling to predict chemical permeability.

In silico models for tissue permeation are commonly either compartmental [12, 13] or diffusion-based [14, 15] that are inexpensive to compute but experience low-fidelity. Compartmental models assume that the chemical concentration in a tissue is homogeneous and governed by an ordinary differential equation in time; physiologically-based pharmacokinetic (PBPK) models generally rely on these for whole-body predictions [16]. Diffusion-based models incorporate spatial variation in chemical concentration but rely on a diffusion coefficient which often represents a homogeneous tissue. Spatially varying diffusion coefficients are possible but any local discontinuities, such as cell boundaries cannot be accounted for directly. Therefore, in both compartmental and diffusive models, each tissue or organ is described by macroscale parameters that must be fitted or approximated. Along with models fitted with machine learning [17, 18], neither are viable for accurate predictions of tissue permeation unless very large datasets are obtained.

In contrast, high-fidelity cell-based models can capture the inherent inhomogeneity of a tissue directly, with existing examples representing hepatocyte spheroids [19] and *in vitro* oral mucosal tissue [20]. Chemical permeation is modelled mechanistically, with diffusion through paracellular routes and/or permeation of cell membranes and transcellular pathways. In particular, the chemical concentration in the tissue is modelled with partial differential equations in multiple spatial dimensions. Whilst cell-based models provide obvious advantages, their adoption has been limited due to their inherent complexity and the necessity of greater computational resources. However, these limitations are diminishing with the availability and affordability of increasing computational power.

Using tissue engineered human buccal mucosa, we previously developed an advanced mechanistic mathematical model of the buccal epithelium [20]. This was used to create a histologically and physiologically-relevant *in silico* model of buccal mucosal chemical permeation using partial differential equations, fitted to chemical permeation from *in vitro* assay data for chemicals with known physiochemical properties [20]. Our previous study also elucidated, for the first time, the influence of convoluted extracellular space on epithelial drug permeation, which was also factored into the *in silico* model, making this a significant improvement on previous models where chemical permeation is likely underpredicted [20]. Moreover, our *in silico* model could be used to make perturbations in, for example, the size of the extracellular spaces to mimic presence of epithelial permeation enhances where this predicted the enhanced permeation of chemicals that pass via the paracellular route [20]. However, this model was based on data generated from tissue engineered *in vitro* buccal mucosal studies. Structural differences between tissue engineered *in vitro* and *in vivo* human tissues, such as size and the number of layers of the keratinocytes in the *stratum spinosum* [20], necessitates the development of a mathematical *in silico* model that can map from *in vitro* to *in vivo*, to enable human-specific chemical permeation predictions.

This current study aims to overcome these problems by generating novel tissue engineered buccal mucosa with reduced permeability barrier properties to better model the buccal mucosa chemical permeability barrier. We further developed a new *in silico* method that maps *in vitro* studies to *in vivo* prediction, where human *in vivo* buccal tissue and cell geometry were included directly so that *in vitro* and *in vivo* differences were accounted. Furthermore, the dual impact of passive membrane transport and the buccal permeability barrier was ascertained. With *in vivo* predictions established, the blood vessel density of the buccal mucosa was assessed using live *in vivo* imaging, and the predictions from the *in silico* model fed into a PBPK model to map whole body chemical distribution. This novel integrated pipeline supports extrapolation from *in vitro* to *in vivo*, potentially improving future compound screening and formulation design for chemicals permeating the buccal mucosa, while reducing reliance on animal tissue.

2. Materials and methods

2.1 *Materials*

All reagents and chemicals were purchased from Merck Life Science UK Ltd (Gillingham, UK) unless otherwise stated.

2.2 Ex vivo oral tissue and in vitro normal oral epithelial models

Immortalised FNB6 buccal keratinocytes [21] were cultured in monolayer as described in [22]. Oral mucosal equivalents (OME) were generated by seeding 5 x 10^5 FNB6 keratinocytes onto collagen IV (7 µg/mL) coated 0.4 µm pore transwell inserts (Greiner Bio-one, Germany). For immature epithelium (immOME), these were incubated for 5 days at air-to-liquid interface, while for fully matured OME (matOME), cells were incubated for 12 days at air-to-liquid interface. *Ex vivo* buccal tissue (four males aged 48, 25, 28, 22 and two females aged 23 and 24, all non-smokers) were sourced from a combination of archived formalin-fixed, paraffin-embedded oral mucosal tissue held by Oral Maxillofacial Pathology, Sheffield Teaching Hospitals NHS Foundation Trust (Ethical approval number 07/H1309/105) and freshly excised buccal tissue from healthy patient volunteers undergoing routine maxillofacial surgery with written, informed consent (Ethical approval number 09/H1308/66).

2.3 Histological analysis of ex vivo and in vitro OME

Normal oral mucosa (NOM) biopsies, immOME, matOME (day 5 and day 12, respectively) were fixed with 10% (v/v) neutral-buffered formalin; alcohol-processed, paraffin wax embedded, 6 µm sections cut using a microtome and sections stained with haematoxylin & eosin (H&E, Epredia, UK). Slides were mounted with distyrene-polystrene xylene (DPX) and imaged under light microscopy. Images were digitised using an Aperio Slide Scanner (Leica). Epithelial thickness measurements were taken using ImageJ software (NIH).

2.4 Immunohistochemical staining of epithelial junctional proteins

Sections of NOM, immOME and matOME were dewaxed, rehydrated and endogenous peroxidase neutralised with 2% hydrogen peroxide for 20 minutes. Antigen retrieval was achieved using Tris and EDTA buffer (pH 9) or 0.01 M citrate buffer (pH 6) at high temperature. After blocking with normal goat serum for 30 minutes, sections were incubated with primary rabbit monoclonal antibody directed to claudin-4 (abcam ab210796, clone EPRR17575) or JAM-1 (abcam ab52647, clone EP1042Y) for 90 minutes at room temperature. After washing, sections were incubated with anti-rabbit biotinylated secondary antibody for 30 minutes at room temperature before a 30-minute incubation with Vectastain ABC reagent (Vector Laboratories, California, USA). Sections were developed with 3,3'-diaminobenzidine tetrahydrochloride (DAB) peroxidase staining kit (Roche, Switzerland) and counter-stained with haematoxylin before mounting with DPX for analysis. An isotype matched IgG antibody (abcam ab172730) was used as a negative control.

2.5 Transepithelial electrical resistance analysis

ImmOME and matOME were stabilised in pre-warmed (36 ± 1°C; PBS pH 7.4) for 20 minutes. The transepithelial electrical resistance (TEER) values were measured using the EVOM2 meter (World Precision Instrument, USA) following Ohm's (Ω) Law. Three TEER values were measured per OME, with a reading from a blank transwell in PBS reading subtracted from the mean account for the insert membrane. Epithelial resistance (Ω cm-2) was calculated using the following equation: TEER = resistance (Ω) x OME surface area (cm^2). OME treated with a 5% sodium dodecyl sulfate (SDS) solution to destroy the permeability barrier, was used as a positive control.

2.6 Buccal epithelium permeation assay

Permeation assays were performed on *in vitro* human buccal mucosa using benzydamine HCl (logP = 3.66), clobetasol-17-propionate (logP = 3.84), oxymetazoline HCl (logP = 3.37) and prochlorperazine dimaleate (logP = 2.86), chosen due to either their current use for treatment of oral mucosal conditions or potential use for oral mucosal delivery. For example, clobetasol-17- propionate for treatment of oral lichen planus, benzydamine as a topical non-steroidal anti-inflammatory drug, prochlorperazine for nausea, and oxymetazoline for Rosacea or regional oral anaesthesia [23-26]. Stock concentrations of clobetasol-17-propionate and prochlorperazine dimaleate were prepared in dimethyl sulfoxide, while oxymetazoline HCl and benzydamine HCl were prepared in a 1:1 v/v ethanol:water mix. Stock solutions were diluted in PBS, pH 7.4 to achieve the final dosing concentration of 1 mg/mL, ensuring that the final concentration of vehicle did not exceed 1% (v/v) to avoid any impact on epithelial viability or barrier integrity. Vehicle only treatment was used as control. immOME and matOME were maintained at 37°C, 5% CO_2 in a humidified incubator and 50 µL of chemical compounds, clobetasol-17-propionate [2.14 mM], oxymetazoline HCl [3.37 mM], benzydamine HCl [2.89 mM] or prochlorperazine-dimaleate [1.65 mM] applied topically to the apical surface of the epithelium for up to 24 hours. After chemical exposure, the receiver PBS (pH 7.4) solution in the basolateral chamber was sampled (200 µL) in a time-dependent manner (for up to 8 hours), and the volume replaced with fresh pre-warmed PBS (pH 7.4) to maintain experimental conditions. The concentration of chemical compounds permeated through the model was determined using high performance liquid chromatography (HPLC).

2.7 UV-high-performance liquid chromatography

Analytical grade chemical HPLC compounds and reagents were used for all experiments. Detection was performed using the Shimadzu prominence HPLC with UV/Vis detection and a XBridge BEH-C18 (4.6 mm x 250 mm), 130 Å pore-size column. Parameters for each chemical were as follows; oxymetazoline-HCl mobile phase consisted of MeCN (40%)/ KH_2PO_4 in 0.1%

$H_3(PO)_4$ (60%) with column eluent monitored at 280 nm. For Clobetasol-17-propionate, the mobile phase was composed of MeCN (70%)/H_2O (30%) with emission detected at 239 nm. Benzydamine-HCl the mobile phase was MeCN (37.5%)/MeOH (37.5%)/$NH_4(CO_3)_2$ [10 mM], (25%), with detection at 308 nm. Prochlorperazine-dimaleate parameters included a mobile phase of CH_3OH (40%)/ H_2O (60%), with detection at 220 nm. All samples were run using an injection volume of 20 µL and flow rate of 1 mL/minute and with sample run times of 10 minutes. Linear regressions were generated and the slope, intercept and correlation coefficient plotted for each standard curve [1-25 µg/mL]. All calibration measurements were conducted in triplicate and a correlation coefficient of 0.99 was obtained for each chemical. Regression statistics were calculated for the lower limit of detection (LoD) and limit of quantification (LoQ) from average results of calibration curves as described in [20]. Quantification of permeated chemicals was deduced considering loss of chemical from the basolateral chamber with each sample taken, as described in [20].

2.8 Optical coherence tomography angiography

Optical coherence tomography angiography (OCTA) was performed on healthy volunteers (with written, informed consent, University of Sheffield ethical approval number 070887) using a multi-beam OCT system (Vivosight, Michelson Diagnostics Ltd, Orpington, Kent, UK) running at a 20 kHz line acquisition rate. This system utilizes a swept-source 1305 nm Axsun laser with a bandwidth of 147 nm, allowing visualization of structures to a depth of ~2 mm into the oral mucosa. OCT angiography was performed as described in [27, 28]. Briefly, four-dimensional (x-y-z-time) OCT volumes were collected from the buccal mucosa. Scans captured a volume of 4 x 4 x 2 mm with 5 repeat B-scans being collected at each y-location. A-scans were acquired with a 10 µm spacing in the x-direction (fast scan) and 20 µm y-direction (slow scan) to provide a balance between imaging speed and high-resolution imaging. Raw data was processed in MATLAB (R2024b – MathWorks) into an angiographic format following a previously described speckle-variance methodology [27]. Motion artefacts were suppressed using a sub-pixel accurate image registration algorithm to an accuracy of 100th of a pixel. A combined wavelet-FFT filter was then utilized to suppress remaining motion artefacts with minimal degradation to the underlying vascular information. Angiographic data was binarized to generate vascular skeletons and this data was used to calculate mean vessel diameter (µm) and vessel density (vessels/mm^2).

2.9 Statistics & data analysis

All data are presented as mean ± SD, with all experimental repeats clearly stated. Parametric data was analysed by ordinary one-way ANOVA with Tukey's post-hoc test for multiple group comparisons. TEER data was analysed using unpaired T-Test with Welch's correction. All

statistical analysis was performed using GraphPad prism, v10.0 (GraphPad Software, San Diego, CA) and significance assumed if $p<0.05$.

2.10 Cell-based in silico models

Three cell-based *in silico* models directly capture the differences in tissue histology for the *in vivo* NOM and *in vitro* immOME and matOME tissues. The *in vitro* models are used to parameterise the *in vivo* model, by fitting two physiologically relevant parameters: cell membrane permeability Q from immOME and the permeability barrier P_B from matOME. The *in silico* models are developed in a similar manner as in [20]; a shorter overview is given here.

Stained tissue sections and histological measurements are used to capture the geometry of the tissue. Nuclei coordinates are inferred and applied in a Voronoi tessellation procedure to determine cell boundaries. The Voronoi tessellation is in a stretched metric so that cells are elongated into the upper spinous strata and superficial layer. Elongation appropriately reflects the ratio of cell widths and heights previously measured in each cell strata. Extracellular spaces are imposed by separating cell boundaries using the polygon offset algorithm; extracellular spaces have differing widths in each cell strata which is taken into account. For the two *in silico* models which match to immOME and NOM, a homogenous superficial layer is isolated. An application layer is added at the top of the epithelium to approximate a chemical droplet or a mucoadhesive film/patch (thickness 442 μm for 50 μL added to a 113 mm² transwell insert). Thus, matOME and NOM have three distinct layers: application, superficial and extra/intracellular (in the spinous and basal tissue layers). The *in silico* model which matches to immOME does not have a superficial layer. The geometry in each case matches experimental measurements of extracellular gap widths; cell widths and heights; and strata thicknesses *in vitro* and *in vivo* [20].

Permeation is inhomogeneous throughout the tissue. Chemicals are assumed to diffuse through the application layer (coefficient D_A), superficial layer (coefficient D_S), intracellular regions (coefficient D_I) and extracellular regions (coefficient $D_E/\tau_S{}^2$),

$$\frac{\partial C_A}{\partial t} = D_A \nabla^2 C_A, \quad \frac{\partial C_S}{\partial t} = D_S \nabla^2 C_S, \quad \frac{\partial C_I}{\partial t} = D_I \nabla^2 C_I, \quad \frac{\partial C_E}{\partial t} = \frac{D_E}{\tau_S^2} \nabla^2 C_E, \tag{1}$$

with concentrations (C_A, C_S, C_E, C_I) and time t. Extracellular diffusion is reduced to account for convoluted subcellular tortuosity τ_S which is $\tau_S = 3.576$ *in vitro* and $\tau_S = 2.188$ *in vivo* [20]. For the mature *in vitro* and the *in vivo* models, concentration and flux are conserved along the boundary between the application and superficial layers,

$$D_A \nabla C_A \cdot n = D_S \nabla C_S \cdot n, \quad C_A = C_S, \quad \text{along the A-S boundary,} \tag{2}$$

(normal n), whereas flux is slowed for passive transport through cell boundaries (coefficient Q) [19],

$$\frac{D_E}{\tau_S^2} \nabla \mathrm{C_E} \cdot n = D_I \nabla C_I \cdot n = Q(C_E - C_I), \quad \text{along the cell boundaries.} \tag{3}$$

Similarly, a permeability barrier is included by assuming slowed transport along the superficial-extracellular boundary,

$$D_S \nabla C_S \cdot n = \frac{D_E}{\tau_S^2} \nabla C_E \cdot n = P_B(C_S - C_E), \quad \text{along the S-E boundary,} \tag{4}$$

The immature epithelial model is assumed to not have a superficial layer or permeability barrier, with conserved concentration and flux from the application layer to the extracellular medium. Also assumed are no loss from the application layer to the environment and lateral symmetry along the tissue (no flux); and a perfect sink at the base of the epithelium (zero concentration). Initially there is only chemical in the application layer.

The application and extracellular regions are approximated to water via the Stokes-Einstein equation [29],

$$D_A = D_E = \frac{k_B T}{6\pi \eta_W R}, \tag{5}$$

with Boltzmann constant $k_B = 1.38065 \times 10^{-23}$ m^2 kg s^{-2} K^{-1}, physiological temperature $T = 310.15K$, dynamic viscosity of water $\eta_W = 6.913 \times 10^{-4}$ kg m^{-1} s^{-1}, and spherical chemical radius R. Molecular mass M and chemical density ρ affect the radius,

$$R = \left(\frac{3M}{4\pi N_A \rho}\right)^{1/3}, \tag{6}$$

with Avogadro's constant $N_A = 6.0221 \times 10^{23}$. Intracellular diffusion is set to the model suggested by [30] for human epithelial cells, along with superficial layer diffusion,

$$D_I = D_S = \frac{D_W}{1.3} \, exp\left[\left(\frac{(4.6\times10^{-9})^2}{20^2} + \frac{(4.6\times10^{-9})^2}{R^2}\right)^{-0.285}\right]^{-1}. \tag{7}$$

Percentage permeated is calculated at each timepoint by integrating the concentration over the entire model ('mass'),

$$\%\, Permeated(t) = 100[1 - m(t)/m(0)\,], \quad m(t) = \int\int C(x,y,t)\mathrm{d}x\mathrm{d}y. \tag{8}$$

2.11 Implementation in silico using EpiPerm™

For each *in silico* model, an initial coarse triangular mesh was produced in MATLAB as an output from Voronoi tessellation. The models were then imported into the C++ library EpiPerm™ [20], which is specifically designed for cell-based models. Superficial and application layers were added by generating elements in EpiPerm™ above the top boundary of the epithelium. The meshes were then refined either: globally; along boundaries such as along cell membranes or at the edges of the domain; or at boundary-vertices such as cell vertices or the corners of the domain. Individual triangular elements were refined by connecting the mid-points of each side, resulting in four sub-elements. Hanging nodes were avoided by dividing neighbouring (unrefined) elements in two. A typical mesh for the NOM model had 1.80 million elements over 0.91 million nodes, with many nodes concentrated near to boundaries and cell vertices, resulting in linear systems with approximately 0.96 million unknowns. The model incorporated approximately 165 biological cells with 5000 mesh nodes or 10000 elements in the vicinity of each cell. A second-order two-dimensional finite-element scheme was adopted in space and forward Euler was applied for time-marching with typical initial time-steps of $\Delta t \approx 60s$. At each time-step, the linear solve phase was undertaken by the sparse parallel linear solver MUMPs [31] under the framework of PETSc, (Portable, Extensible Toolkit for Scientific Computation) [32]. The linear solve phase was therefore parallelisable over multiple compute threads, but the construction and storage of the linear system was serial.

2.12 Parameterising cell-based models using in vitro results

The *in vivo* cell-based model was parameterised from *in vitro* experiments. First, an *in silico* model that mimics permeation of immOME was fitted to experimental measurements of percentage permeated to deduce cell-membrane permeability Q. Second, the cell-membrane permeability Q was applied in a second *in silico* model which mimicked matOME, to fit the magnitude of the permeability barrier P_B. In both cases the fitting was undertaken by minimising the L2 norm between the *in silico* and *in vitro* percentage permeated results using Newton iteration. Finally, the two permeability parameters Q and P_B were applied in the *in vivo* model.

2.13 Encoding cell-based predictions as whole-epithelium permeability coefficients

A compartmental model assumes that the epithelium is homogeneous. Chemical concentration C is subject to,

$$\frac{dC}{dt} = -KC/L, \quad C(t=0) = C_0, \tag{9}$$

(thickness L) with permeability coefficient $K > 0$. The percentage permeated in the compartmental model is given by,

$$\%\, Permeated(t) = 100(1 - C(t)/C_0) = 100(1 - e^{-Kt/L}), \tag{10}$$

and this is fitted to *in vivo* percentage permeated predictions via Newton iteration in K.

2.14 Coupling in silico permeation models to a generic PBPK model

The generic PBPK model first described by Peters [16] was extended to include an oral mucosal compartment and allow for the coupling of the *in silico* permeation models to a conventional PBPK model. The extension comprises an additional tissue compartment representing the vascularised component of the oral mucosa (lamina propria), and the dynamics of chemical concentration in this tissue (C_{OM}) are given by:

$$\frac{\mathrm{d}C_{OM}}{\mathrm{d}t} = \frac{Q_{OM}}{V_{OM}}\left(C_{AR} - \frac{C_{OM}R}{f_{u(p)}K_{p,u(OM)}}\right) + \frac{1}{V_{OM}}\frac{\mathrm{d}M_{OM_{epi}}}{\mathrm{d}t}, \tag{11}$$

where Q_{OM} and V_{OM} represent blood flow and volume for this tissue. Tissue distribution parameters impacting the local concentration include the blood:plasma concentration ratio (R) fraction of chemical unbound in plasma ($f_{u(p)}$); and the tissue partition coefficient used to represent the ratio of (steady-state) tissue concentration and the (steady-state) concentration of unbound chemical in the plasma ($K_{p,u(OM)}$). The supply of chemical into the lamina propria tissue is determined by both systemic concentrations in the arterial compartment (C_{AR}) and delivery via permeation across the oral mucosal epithelium, $\frac{\mathrm{d}M_{OM_{epi}}}{\mathrm{d}t}$; the latter is where the PBPK and *in silico* permeation models are coupled. This variable can either be derived directly from the output of the cell-based oral mucosal model, as in Fig 5, or, for the compartmental oral mucosal model described in supplementary figure 4A-D, can be explicitly integrated within the PBPK system of equations, as

$$\frac{\mathrm{d}M_{OM_{epi}}}{\mathrm{d}t} = -\frac{K}{L_{OM_{epi}}}M_{OM_{epi}}, \tag{12}$$

Where K is the permeability coefficient and $L_{OM_{epi}}$ represents the thickness of the epithelium (0.057121 cm); corresponding results are shown in supplementary figure 5. Blood flow within the lamina propria was set to 82.83 mL/h [33]. The volume of the lamina propria compartment

(V_{OM}) was estimated to be 11.76 mL from the average human oral mucosal surface area of 214.7 +12.9 cm², measured by [34], and the lamina propria thickness of 597.3 ± 93.0 µm, measured from normal human oral mucosa sections in this study. The lamina propria was assumed to be a perfect sink from the oral mucosal epithelium.

The generic PBPK model requires specific inputs to simulate the pharmacokinetics of each chemical. These include physicochemical properties (MW, pKa, logP) and common absorption, distribution, metabolism and excretion (ADME) parameters (blood:plasma concentration ratio, R; fraction unbound in the plasma, $f_{u(p)}$; and intrinsic clearance, CL_{int}). Measurements of the former category were obtained from DrugBank (https://go.drugbank.com), while the latter were approximated *in silico*. The QSAR software, OPERA [35] was used to predict CL_{int} and $f_{u(p)}$ based on chemical structure, while the blood:plasma concentration ratio was calculated based on the method of Rodgers & Rowland [36], using logP, pkA, and $f_{u(p)}$ as inputs (Supplementary Table 1).

2.15 Encoding cell-based predictions as whole-epithelium diffusion coefficients

The diffusion model (supplementary Fig. 4) is one-dimensional with an application layer (coefficient D_A, thickness L_A) and an epithelial layer (coefficient D, thickness L), such that,

$$\begin{gathered}\frac{\partial C_A}{\partial t} = D_A \frac{\partial^2 C_A}{\partial x^2}, \quad \frac{\partial C_A}{\partial x}(x=0) = 0, \\ C_A(x=L_A) = C(x=L_A), \quad \frac{\partial C_A}{\partial x}(x=L_A) = \frac{\partial C}{\partial x}(x=L_A), \\ \frac{\partial C}{\partial t} = D \frac{\partial^2 C}{\partial x^2}, \quad C(x=L_A+L) = 0.\end{gathered} \tag{13}$$

Chemicals diffuse through the application layer with no loss to the environment and through the epithelial layer to a perfect sink at the base. The application layer thickness and diffusion coefficient match the cell-based model and the epithelial thickness L matches to that measured *in vivo* data [20]. Initially there is only chemical present in the application layer. The diffusion model is solved numerically with a second-order finite-difference scheme and implicit-Euler time marching in MATLAB. Fitting in D is undertaken with Newton iteration.

3. Results

3.1 In vitro modelling of the oral mucosal permeability barrier

To model the permeability barrier effect of oral mucosa, two types of human buccal epithelium were tissue engineered; a 12-day cultured oral mucosal equivalent (OME) to represent a mature oral epithelium (matOME) with a fully formed permeability barrier and a 5-day cultured

OME to represent an immature oral epithelium (immOME) with impaired barrier function. matOME and immOME were validated against healthy human buccal NOM for histological structure, tight junction localisation and functional permeability using *in vitro* transwell permeation assays.

Histological analysis of tissue sections shows that NOM exhibited a stratified squamous epithelium consisting of a single layer of columnar-shaped basal cells that attach apically to the basement membrane. On top of the basal layer sits the *stratum spinosum*, consisting of several layers of polygonal-shaped keratinocytes that are topped apically by a superficial layer consisting of flattened, differentiated keratinocytes (Fig 1A). The *stratum corneum* was absent because unlike skin, buccal mucosa is non-keratinised, with the superficial layer of keratinocytes retaining their cell nuclei (Fig. 1A). matOME replicated this histological organisation but were significantly thinner (225 ± 9 µm) than NOM (571 ± 79 µm) due to the reduced thickness of the *stratum spinosum* (Fig. 1A&B). In contrast, immOME displayed significantly thinner epithelium (113 ± 7 µm), a poorly defined basal cell morphology, disorganised stratification and differentiation, and absence of a superficial layer (Fig. 1A&B).

Tight junction expression mirrored these structural differences. In NOM and matOME, claudin-4 was localised predominantly to the plasma membranes of keratinocytes in the upper *stratum spinosum,* just below the superficial layer, consistent with a functional permeability barrier (Fig. 1A). In contrast, claudin-4 localisation in immOME was diffuse and deeper into the *stratum spinosum*, with evidence of cytoplasmic staining. Similar differences between matOME and immOME were observed for JAM-1 immunostaining (Fig. 1A), indicating that the tight junction and therefore permeability properties of immOME are compromised compared to matOME.

Barrier function was quantified by TEER, a technique used to measure the tissue electrical resistance associated with cell barrier integrity and permeability of epithelial tissue [37]. High TEER values indicate robust tight junction integrity and low tissue permeability whereas low values indicate poor tight junction function and high tissue permeability [38]. TEER values for matOME were significantly greater than those for immOME (1858 ± 585 $\Omega \cdot cm^2$ compared to 528 ± 35 Ω·cm-2, $p<0.01$) (Fig. 1C), consistent with robust versus deficient barrier properties. Functional assays corroborated these findings. Following topical application of the small lipophilic molecule, clobetasol-17-propionate (0.467 kDa, LogP 3.84) for 4 hours, 98 ± 1% of the chemical permeated immOME whereas only 15 ± 4% permeated matOME ($p<0.001$; Fig. 1E). These large differences demonstrate that immOME is highly permeable with diminished transcellular and paracellular barriers. Collectively, these data show that OME can be engineered to exhibit an intact, mature permeability barrier (matOME) or an epithelium largely devoid of a permeability barrier (immOME).

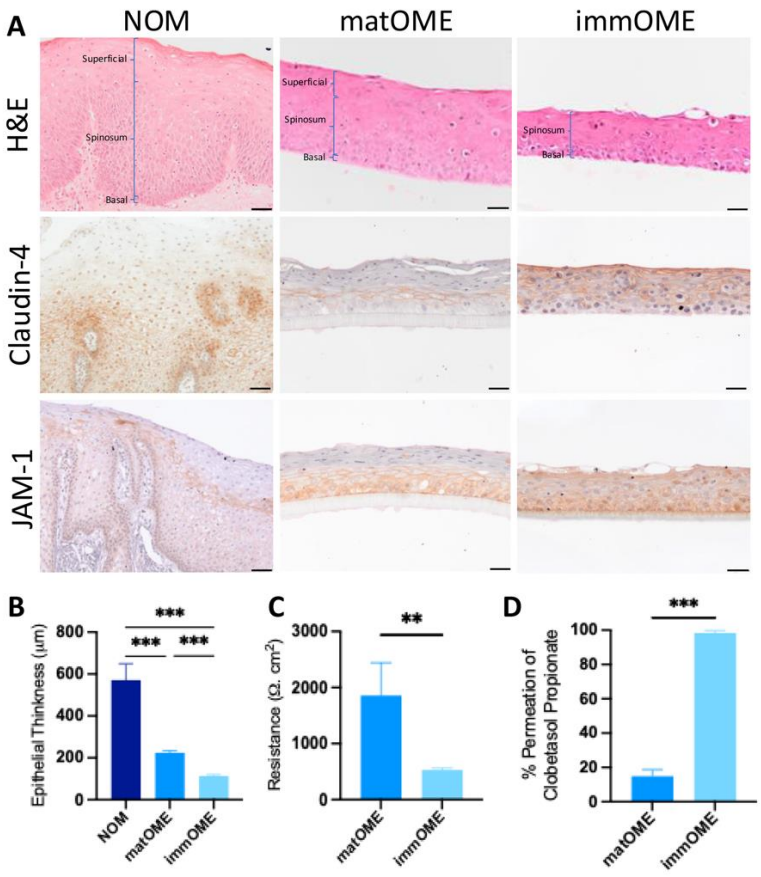

Figure 1. Characterisation of mature and immature human oral mucosal equivalents. Representative images of H&E and immunohistochemically-stained tissue sections for the tight junction proteins, claudin-4 and JAM-1 on NOM, matOME and immOME; scale bar = 50 µm (A). Epithelial thickness of NOM, matOME and immOME (n=9) (B). TEER measurements of matOME and immOME (n=5) (C). Permeation of clobetasol-17-propionate across matOME or immOME for 4 h (n=6) (D). Data are presented as mean ± SD, statistical analysis was performed using an one-way ANOVA with Tukey's post-hoc test for multiple comparisons (B) or Student's t-test (C&E) where **P<0.01 and ***p<0.001.

3.2 Cell-based in silico models capture the histology of in vitro tissue

Previously, we developed a prototype *in silico* model of *in vitro* oral mucosal epithelium that captured the tissue histology but lacked an explicit permeability barrier, limiting *in vitro* to *in vivo* extrapolation [20]. Herein, we constructed three cell-based mechanistic models: two emulating chemical permeation through *in vitro* immOME and matOME tissues, respectively, and one emulating *in vivo* NOM. These capture the dual impact of tissue histology and the permeability barrier on overall oral mucosal chemical permeability.

By adopting a cell-based *in silico* approach the histology of oral tissues was captured directly (Fig. 2A-D). H&E-stained tissue sections from a biopsy of human buccal mucosa (Fig. 2A) were used as templates to indicate cell nuclei coordinates (Fig. 2B), from which cell boundaries were generated computationally using a Voronoi tessellation procedure (Fig. 2C). The tessellation is undertaken in a stretched Euclidean metric to account for cell elongation from the basal to the upper spinous and superficial layers. Extracellular spaces were then imposed with a polygon offset algorithm (Fig. 2D). *in silico* model geometry (extracellular space width, cell sizes, cell layer thicknesses used in the stretched Euclidean metric) matched measurements of *in vivo* buccal mucosa (measured in [20]). Analogous *in silico* models were designed to match *in vitro* generated tissues using *in vitro* measurements for matOME (Fig 2E) and immOME (Fig. 2F, see Supplementary Fig. 1 for further details).

The cell-based models implicitly include the inhomogeneity of permeation through oral epithelium. At the start of the computation, chemicals were applied to the surface of the epithelium in an application layer. As time increased the chemicals diffused through the application and superficial layers with no loss to the environment (diffusion coefficients D_A and D_S). The chemicals then permeated through the permeability barrier that begins at the top of the *stratum spinosum* layer with a permeability coefficient P_B applied as a boundary condition. If $P_B = 0$ then no chemical could permeate into the spinous layer and if $P_B \to \infty$ then there was no permeability barrier between the layers. Within the *spinosum* and basal layers, paracellular and transcellular permeation was handled with diffusion through extracellular spaces and intracellularly with coefficients D_E/τ_S^2 and D_I, respectively. We previously showed that the tortuosity of extracellular spaces increases the cellular surface area, resulting in more uptake through cells, but lengthens the extracellular pathways, slowing permeation around cells [20]. These effects were accounted for without extra computational expense by appropriately scaling the extracellular diffusion coefficient by subcellular tortuosity τ_S. Chemicals were assumed to permeate through cell membranes with passive transport, with a permeability coefficient Q applied along the cell membranes. If $Q = 0$ then chemicals did not permeate into cells. At the base of the epithelium a perfect sink was applied, to mimic chemical permeation to a large volume of media *in vitro* or to the systemic circulation *in vivo*.

Incorporating multiple *in silico* parameters, each representing a different physical phenomenon, was useful as some of the parameters could be approximated, such as diffusion in the application and superficial layers and in the paracellular and intracellular regions. The diffusion coefficients were approximated from a chemical's molecular mass, size and density. The only parameters that could not be approximated *a priori* were the passive transport coefficient Q and the permeability barrier coefficient P_B.

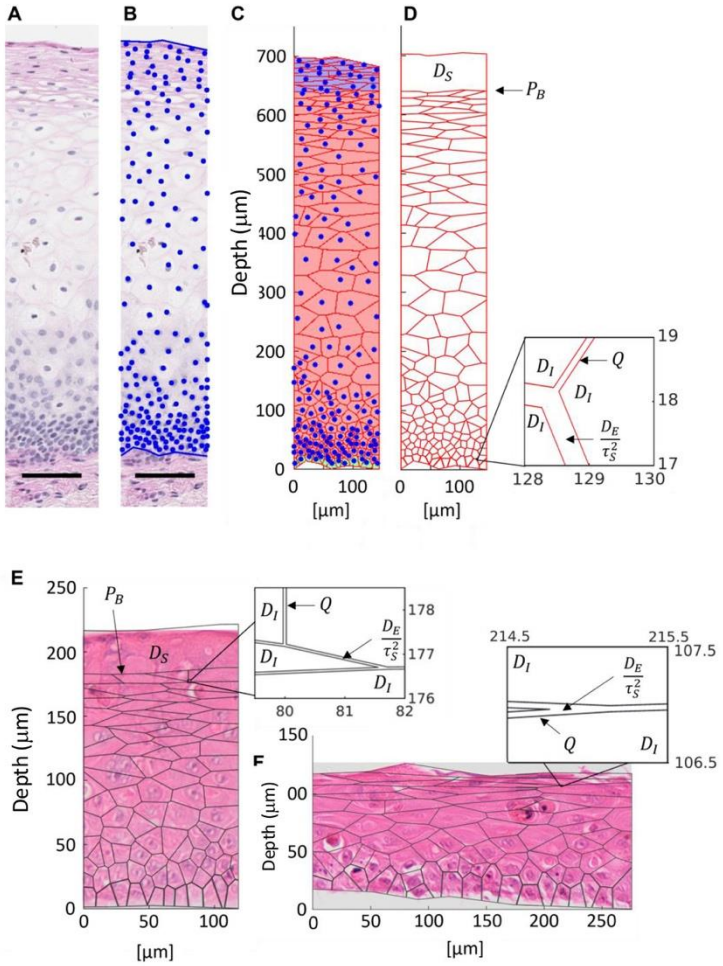

Figure 2. Histological sections of oral mucosa parameterise *in silico* models of chemical permeation. H&E-stained NOM (A) indicated nuclei coordinates and tissue boundaries (B). Extracellular spaces were imposed using Voronoi tessellation to match measurements undertaken in [20] (C). The resulting model incorporates: superficial layer diffusion D_S, extracellular diffusion D_E including subcellular tortuosity τ_S, intracellular diffusion D_I, a permeability barrier P_B, and membrane transport Q (D). A diffusive application layer is also applied atop the epithelium (not shown). *In silico models* of matOME (E) and immOME (F).

3.3 In vitro permeation assays parameterise in-silico models

To evaluate chemical permeation across OME with differing barrier integrity, four lipophilic chemical compounds (oxymetazoline HCl (logP = 3.37, 3.4 mM), benzydamine HCl (logP = 3.72, 2.9 mM), clobetasol-17-propionate (logP = 3.84, 2.1 mM) and prochlorperazine dimaleate salt (logP = 4.53, 1.6 mM)) were applied topically onto immOME or matOME. Receiver-phase concentrations were quantified by HPLC overtime (Fig. 3A) and the cumulative % permeated through *in vitro* epithelium calculated for each compound. Across all

compounds, immOME was more permeable than matOME (Fig. 3B-E). Both oxymetazoline HCl and clobetasol-17-propionate permeated immOME by over 90% within 6 hours, whereas prochlorperazine and benzydamine HCl showed slower permeation at 68.4% and 50.3%, respectively (Fig. 3B-E). The permeation profile of oxymetazoline HCl demonstrated a biphasic profile with a slow initial phase followed by rapid permeation from 2 hours onwards (Fig. 3B). In contrast, matOME limited permeation of all chemicals to <50% at 6 hours, consistent with a well-formed permeability barrier. Clobetasol-17-propionate permeated 42.2%; prochlorperazine 30.5% and benzydamine HCl 29.2% (Fig. 3C-E). Oxymetazoline HCl permeated 16.6% at 5 hours but 49.5% at 6 hours; this sudden uptick was excluded from later *in silico* fitting (Fig. 3B). In both immOME and matOME, the permeation rate did not correlate with lipophilicity (logP). At 24 hours, the percentage permeated had still not reached over 90% for some chemicals (benzydamine HCl 63.2% (immOME) and 33.5% (matOME), clobetasol-17-propionate 67.1% (matOME), and prochlorperazine 65.6% (matOME) indicating that xenobiotic metabolism or tissue retention had potentially occurred.

Cell-based *in silico* models which emulate permeation of immOME and matOME were fitted to the experimental results (Fig. 3B-E), to capture the *in silico* passive transport coefficient Q and permeability barrier coefficient P_B. Xenobiotic metabolism was not included due to insufficient quantitative data on enzyme activity in buccal tissue. First, the immOME permeation data was used, because it lacks both a superficial layer and a functional permeability barrier, its permeation profile predominantly reflects passive transport whereby the only hindrance to permeation is the rate at which chemicals permeate cell membranes. The passive transport coefficient Q was determined for each chemical: oxymetazoline HCl $Q = 5.13\,x\,10^{-7}\mathrm{ms}^{-1}$, benzydamine HCl $Q = 4.05\,x\,10^{-7}\mathrm{ms}^{-1}$, clobetasol-17-propionate $Q = 1.67\,x\,10^{-6}\mathrm{ms}^{-1}$, and prochlorperazine $Q = 6.86\,x\,10^{-7}\mathrm{ms}^{-1}$. The percentage permeated over time predicted by the immOME *in silico* model (Fig. 2E) was fitted to immOME *in vitro* data by iterating in □ until the difference between the predicted and measured results was at a minimum. The fit from the immature *in silico* model was good in all cases except oxymetazoline HCl, which had a slightly different permeation profile than the model predicted. As the *in silico* model includes the tissue histology, it also predicts the inhomogeneous chemical concentration throughout the epithelium (for example, see supplementary figure 2 for clobetasol-17-propionate).

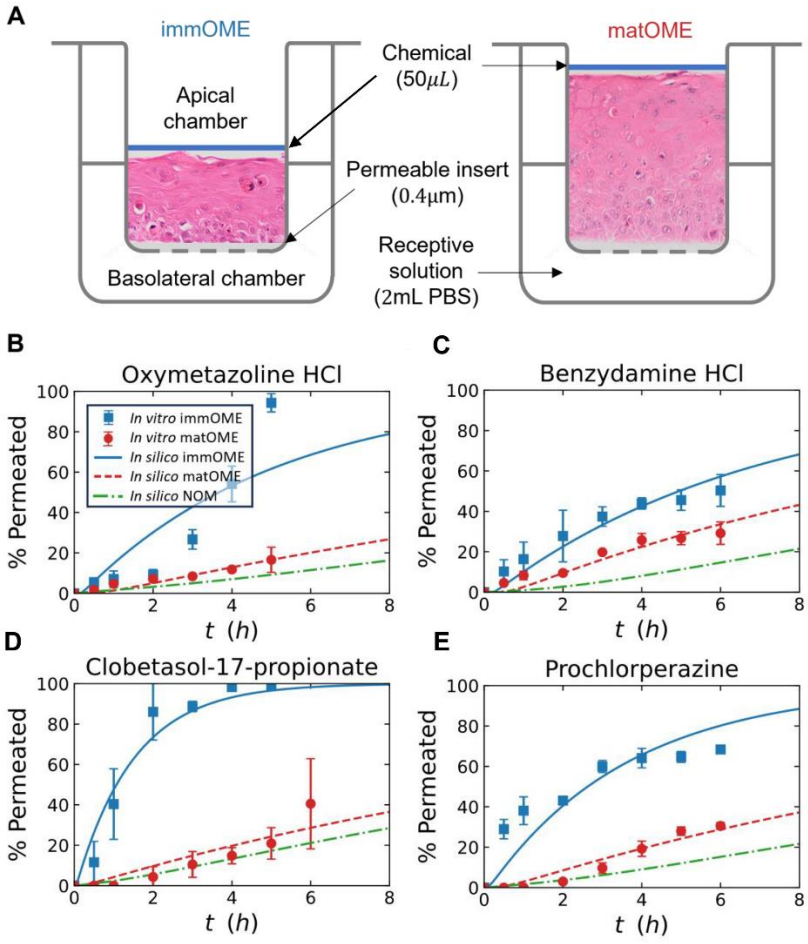

Figure 3. Translation from *in vitro permeation to in vivo predictions*. *In vitro* permeation assays using 50 µL of chemical applied topically to either immOME or matOME with a surface area of 113 mm². A basolateral chamber containing 2 mL of PBS was used as a receptive solution sink and permeation of chemical into the sink was measured by HPLC overtime (A). Membrane permeability Q and the permeability barrier P_B were captured from immOME (Blue) and matOME (Red) permeation data (mean ± SD) and applied in an *in silico* model of NOM for *in vivo* (Green) predictions (B).

MatOME, which contains a superficial layer and an established permeability barrier was incorporated in the matOME *in silico* model (Fig. 2F). Predicted percentage permeated from this model was fitted to matOME *in vitro* data to determine the permeability barrier coefficient P_B for each chemical: oxymetazoline HCl $P_B = 8.74 \times 10^{-9}\text{ms}^{-1}$, benzydamine HCl $P_B = 6.38 \times 10^{-8}\text{ms}^{-1}$, clobetasol-17-propionate $P_B = 8.93 \times 10^{-9}\text{ms}^{-1}$ and prochlorperazine $P_B = 1.28 \times 10^{-8}\text{ms}^{-1}$. In this case, the *in vitro* permeation profile was well captured for every chemical. Together, these chemical-specific parameters provide a mechanistic basis for translating *in*

vitro permeation behaviour to *in vivo* predictions when applied to the native geometry of human oral buccal mucosa.

3.4 Translation from in vitro to in vivo predictions

To translate from *in vitro* to *in vivo*, an *in silico* model of *in vivo* oral mucosa was parameterised with the *in vitro* permeation parameters (Fig. 2D) along with multiple assumptions. It was assumed that: (1) there was no difference in passive transport along cell membranes between *in vitro* and *in vivo* tissues, (2) the strength of the oral mucosal permeability barrier *in vivo* was the same as matOME, (3) diffusion through the intracellular and extracellular spaces was the same as *in vitro*, and (4) the lamina propria was as a perfect sink, with the chemical concentration in the blood being much smaller than the epithelium.

With these assumptions, the mapping from matOME to NOM is undertaken by accounting for their differences in histology: the thicker epithelial strata of NOM; the different cell shapes and sizes; and the different geometry of the extracellular spaces, as measured in [20]. *In vivo* predictions are shown in Fig. 3B-E (green lines). *In vivo* tissue was predicted to be less permeable for all compounds than in *in vitro* cultured OME, due to its increased epithelial thickness, especially in the *stratum spinosum*. After 6 h, predicted % permeated *in vivo* was: Clobetasol-17-propionate (21.1%), followed by prochlorperazine (15.2%), benzydamine HCl (14.6%) and oxymetazoline HCl (11.5%) (Fig. 3). The dual impact of passive transport and the oral mucosal permeability barrier are highlighted upon comparing the predictions for each chemical. For example, given that clobetasol-17-propionate and oxymetazoline HCl permeated immOME relatively quickly thus suggesting quick passive transport through cell membranes, the difference between their *in vivo* predictions and matOME *in vitro* data is lessened relative to benzydamine HCl and oxymetazoline HCl, which had slower immOME permeation. The importance of the permeability barrier is further demonstrated in supplementary Fig. 3, in which the permeability coefficient P_B of clobetasol-17-propionate is increased (weaker permeability barrier) or decreased (stronger). The permeation *in vivo* is strongly affected, for example with 70% permeated after 6 hours with a very minimal permeability barrier (weakened with coefficient $100P_B$). Passive transport through cell membranes has a lesser impact, as shown by a similar analysis with the cell-membrane permeability coefficient Q.

To encode the predicted permeation data *in vivo* in a manner that may be useful to the wider research community, and to make comparisons with existing data for skin, whole-epithelium permeability coefficients K (related to absorption rate constants as $k_a = KL$) and whole-epithelium diffusion coefficients D were determined from the cell-based *in silico* results

(supplementary Fig. 4). Here it is stressed that the permeability coefficients and diffusion coefficients are only to encode the cell-based predictions and do not represent an alternative to the cell-based model. The coefficients were either determined using the first 8 hours of chemical permeation from the *in vivo* cell-based model or the whole time. Permeability coefficients K are shown in supplementary Fig. 4D for each chemical against lipophilicity (logP). There was a slight non-monotonic upward trend in permeability with lipophilicity. Fitted to 8 hours, the line of best fit with logP was

$$K = 0.0003521 \times logP + 0.0001817 \quad (14)$$

with R^2=0.145. Whole-epithelium diffusion coefficients D are depicted in supplementary Fig. 4H for each chemical and a comparison with diffusion coefficients measured in skin epidermis [39] is made. The oral mucosal diffusion coefficients determined herein are greater than most other compounds tested in skin epidermis, suggesting that oral mucosal tissue is more permeable than skin (if at the same thickness).

3.5 Systemic chemical delivery and physiologically-based pharmacokinetic coupling

Chemicals permeating the buccal mucosa will enter the subepithelial microvasculature that feeds into the systemic circulation. Therefore, in addition to *in silico* tissue permeation predictions, PBPK modelling to predict whole-body chemical distribution and clearance is required, however, published data on the vascularity of buccal mucosa is sparse. Histological analysis of human buccal mucosa tissue shows the presence of numerous small blood vessels within 50 μm of the basal layer of the buccal epithelium (Fig. 4A). Optical coherence tomography angiography (OCTA) allows real-time visualisation of the subepithelial vascular plexus (blood vessels beneath the epithelium) to a depth of 2 mm. OCTA C-scans from human buccal mucosa detected blood flow in blood vessels within the lamina propria (Fig. 4B). More detailed analysis shows an extensive vascular plexus network of small and larger vessels. The mean vessel density per image was 28.9 ± 11.5% with mean vessel diameter of 68.4 ± 27.6 μm (Fig 4C). Structural image analysis in three-dimensions showed numerous capillary loops emanating from vascular plexus into the lamina propria, terminating close to the epithelial basal cell layer (Fig 4D, and video in supporting material) representing real-time imaging of the blood vessels highlighted in Fig. 4A. The capillary loop depth was 78.2 μm while the subepithelial vascular plexus depth was 232.9 μm.

Using the available data on vascularity, we coupled the predicted permeation of *in vivo* oral mucosal epithelium (from the cell-based model) to a generic PBPK model [16], extended to include and the lamina propria (where the vasculature is located), to simulate whole-body

chemical distribution. When the predicted pharmacokinetics of the four different chemicals via PBPK modelling are compared, there were differences in the tissue-specific outputs that depend not only on delivery via oral mucosal absorption but also on chemical protein binding and the specific properties of each chemical (Fig. 5). For example, clobetasol-17-propionate has the fastest permeation through the oral mucosal epithelium (Fig. 5A), leading to high predicted concentrations in the lamina

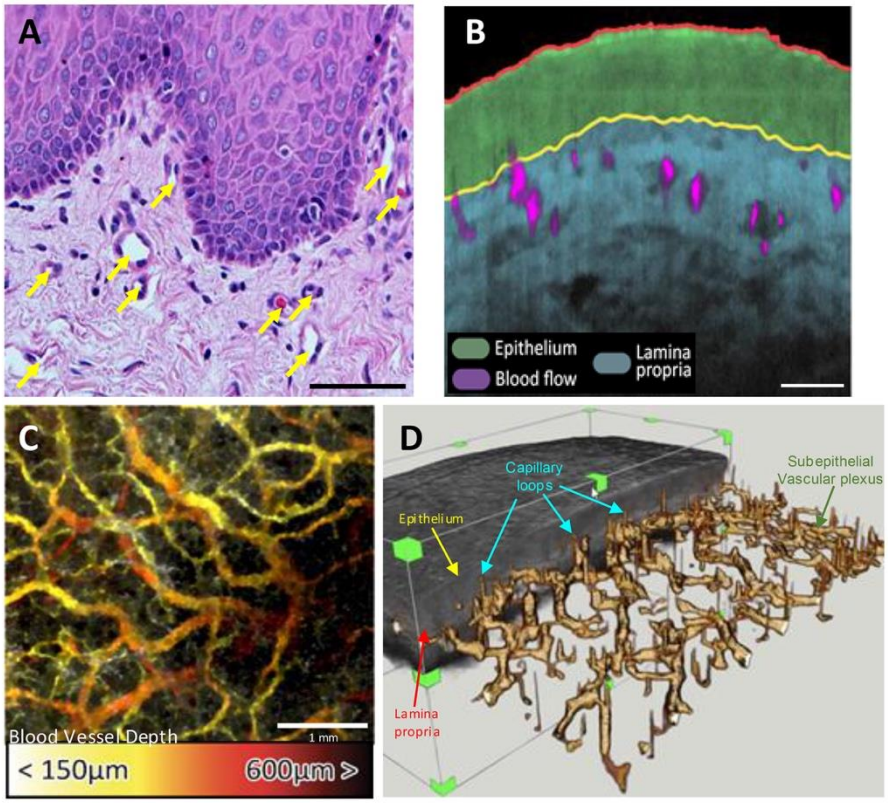

Figure 4. Histology and optical coherence tomography angiography show the extensive vascular network at the submicron level beneath the oral epithelium. H&E-stained section of human NOM showing different sized blood vessels (yellow arrows) within the lamina propria close to the basal cells and rete ridges of the epithelium (erythrocytes can be observed within some vessels). Scale bar = 50 μm (A). OCT real-time beta-scan of NOM showing active blood flow (magenta) within the subepithelial vascular plexus. Scale bar = 200 μm (B). OCT angiography of the submicron vascular network beneath the buccal epithelium showing vessel depth and diameter. Scale bar = 1 mm (C). OCT 3D render showing the complete subepithelial vascular plexus (green arrow) within the lamina propria (red arrow) running at the submicron level under the buccal epithelium (yellow arrow). Capillary loops can be seen raising vertically from the vascular plexus to terminate between the epithelial rete ridges (D). A reconstruction video of the image shown in (D) can be found in the supplementary material.

propria, but relatively low concentrations in blood. However, clobetasol-17-propionate is a lipophilic neutral chemical and therefore is preferentially distributed into tissues, particularly lipid-rich tissues such as adipose and brain, with low levels predicted in the heart and liver (Fig. 5B). Prochlorperazine is even more lipophilic (higher logP; which strongly drives predicted adipose levels) but is ionisable (as a base with pKa of 8.1), causing a more nuanced effect on other tissue partitioning, and a higher degree of plasma protein binding in the venous blood (i.e., lower predicted $f_{u(p)}$; generally confining more chemical to the blood when all else is equal) (Fig. 5B). Oxymetazoline displays lowest absorption and is cleared quickly from the lamina propria and into the venous blood and is then preferentially located in the liver rather than other tissues (Fig. 5A-B). The four chemicals are relatively similar (e.g., narrow range of logP; 3 out of 4 are bases with similar ionic strength, etc.) with generally high tissue distribution and slow clearance, so the predicted differences in kinetics are subtle, but can be explored by examining the input properties and model equations. The calculation of tissue partitioning for example (using the Rodgers & Rowland method for this PBPK model [36, 40]), is a key determinant driving the observed differences in relative tissue concentrations.

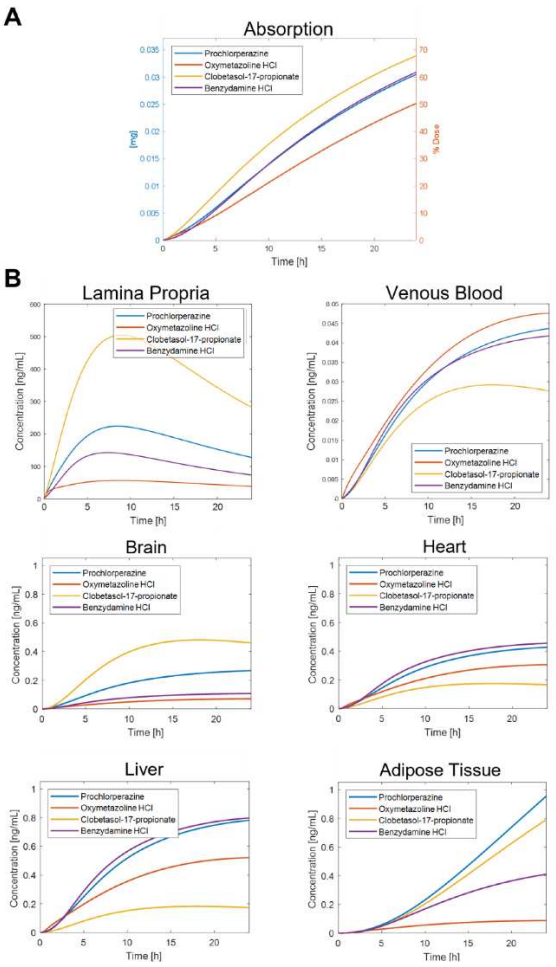

Figure 5. Temporal absorption and tissue response predicted by PBPK modelling following topical application of four chemicals to the oral buccal mucosa. *In vivo* predictions from the *in silico* model (A) are used as input to the generic PBPK model described by Peters (2008), to predict chemical concentration in an additional lamina propria compartment and, among others, the venous blood, brain, heart, liver and adipose tissue (B).

3.6 Validation of the coupled oral mucosal PBPK model for prochlorperazine

To validate our coupled oral mucosal-PBPK modelling approach, the model was applied to prochlorperazine administered via both intravenous and buccal routes, allowing evaluation of the model's predictive performance against independent *in vivo* pharmacokinetic data, and to demonstrate its applicability for predicting systemic exposure following buccal administration. Initially, the PBPK model for prochlorperazine was calibrated by fitting it to published pharmacokinetic data from intravenous administration [41]. This calibration step enabled independent validation of the oral absorption component against buccal administration kinetics, separate from systemic pharmacokinetics (distribution and elimination). Default PBPK input parameters, obtained via QSAR predictions, were optimised to more accurately reflect the intravenous pharmacokinetics following a 12.5 mg dose [41]. Metabolism and plasma binding parameters were adjusted to better match *in vivo* kinetics while remaining consistent with known ADME characteristics. Specifically, the default fraction of unbound drug in plasma ($f_{u(p)}$) was increased from 0.03 to 0.2 (still within the expected range for a highly-bound, lipophilic drug with a high volume of distribution). The intrinsic clearance parameter was also adjusted to 50 µL/minute/10^6 cells to reflect the known high clearance of prochlorperazine [42]. The calibrated PBPK model is compared with the Isah *et al*. study in Fig 6A.

Next, the coupled oral mucosal-PBPK model, using the calibrated parameters, was simulated for buccal absorption with a 6 mg dose of prochlorperazine and compared to data on prochlorperazine plasma levels found in humans over 48 h following placement of a 6 mg mucoadhesive tablet between the gingival and labial mucosa [43]. While the initial absorption phase of the simulated pharmacokinetics closely resembled the *in vivo* study, the model predicted relatively higher peak concentrations and overall exposure (Fig 6B). This discrepancy likely stems from differences in the administration methods. The oral mucosal-PBPK model simulated complete absorption of the 6 mg dose of a fixed mucoadhesive patch adhered to the buccal mucosa for 24 h. In contrast, the *in vivo* study utilised an adhesive tablet that was expected to remain in place for only 1 to 2 h [43].

The model was able to more closely recapitulate the *in vivo* plasma data reported by Finn *et al.* [43] by accounting for these differences in application. This was achieved either by reducing the absorption phase to 5 h (Fig 6C) or by reducing the absorption phase to 2 h (to match the expected tablet residence time), while simultaneously increasing the permeability rate (to account for the bidirectional absorption expected from a tablet positioned between the labial and gingival mucosa) (Fig 6D). In both instances the plasma concentrations were similar for model and *in vivo* data. This validation demonstrates that the coupled oral mucosal-PBPK modelling framework can successfully predict systemic exposure following buccal administration of prochlorperazine.

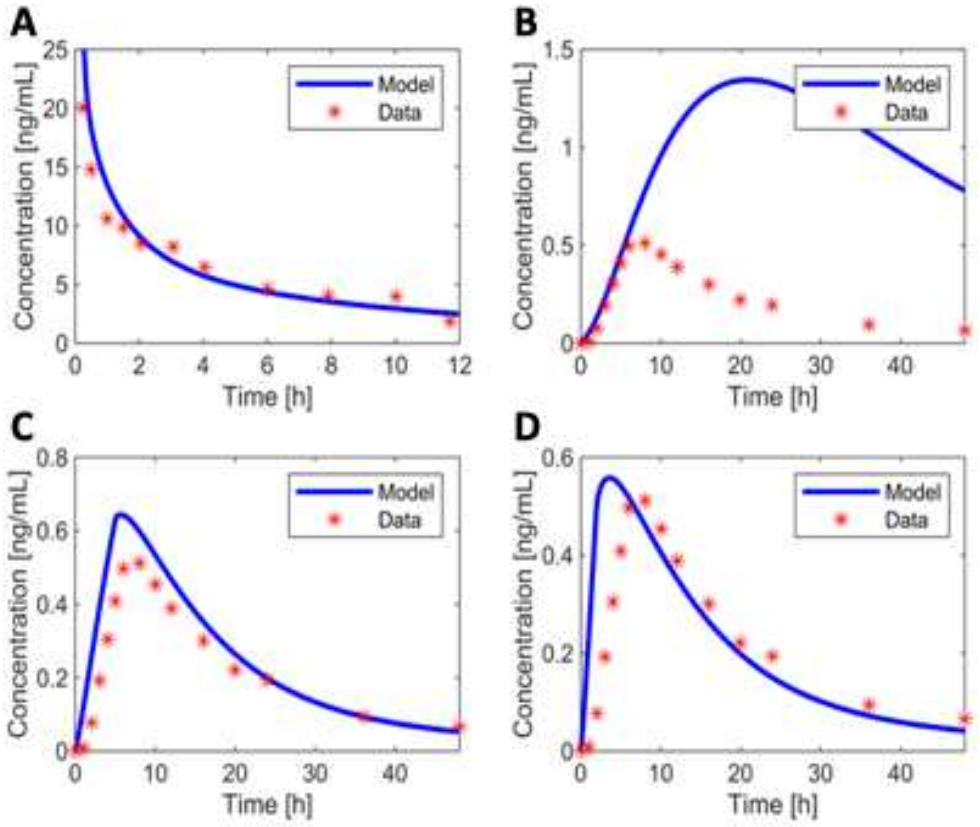

Figure 6: Validation of the in PBPK model for prochlorperazine. Comparison of the calibrated PBPK model for prochlorperazine with plasma concentration *in vivo* data [41], depicting the pharmacokinetics after a 12.5 mg intravenous dose (A). Comparison of the coupled oral mucosal-PBPK model for plasma pharmacokinetics of prochlorperazine (calibrated with intravenous data) simulating 6 mg of drug applied by mucoadhesive oral patch to the buccal mucosa with *in vivo* data using a 6 mg buccal tablet inserted between the labial and gingival mucosa designed to remain in place for 1 to 2 h [43] (B). Plasma concentrations when: Absorption period is reduced and permeability stopped after 5 h, (C) and absorption period reduced to 2 h to match expected tablet residence time, and the permeability rate is increased to account for increased permeability from the labial and gingival mucosa, with permeability rate doubled (D).

4. Discussion

The uptake of human *in vitro* models for chemical screening, coupled with the recent commitment by the U.S. Food and Administration (FDA) to phase out the reliance on animal testing [44], has intensified the need for robust *in silico* methods that translate *in vitro* measurements into *in vivo* human predictions. However, the challenge of accurately extrapolating *in vitro* data persists, with the industry standard currently to scale compartmental parameters using fits to, for example, animal body weight [45, 46], an approach that lacks mechanistic fidelity and cannot fully account for human epithelial architecture.

Cell-based *in silico* models offer an alternative with improved predictability due to the inclusion of tissue histology. Previous cell-based models have been developed to capture chemical permeation in hepatocyte spheroids [19] and engineered *in vitro* oral mucosal tissue [20], but no approach has yet linked *in vitro* buccal permeation to *in vivo* human predictions. Here, we present the first integrated workflow in which iterative *in vitro* experimentation is used to parameterise a mechanistic cell-based model that can translate permeation behaviour from engineered tissue to native human buccal mucosa.

The type of tissue used to generate permeation data to parameterise *in silico* modelling is extremely important. There is insufficient post-surgical *ex vivo* human oral mucosa for laboratory experimentation [47]. Rodent buccal mucosa is keratinized, more resembling skin and is therefore unsuitable [48]. Porcine oral mucosa most closely mimics human tissue, but here there are issues with subtle differences in tissue structure, inter animal variability and ethical and cultural concerns limiting its use [48, 49]. Tissue engineered buccal mucosa overcomes these limitations and is now frequently used as a replacement for animal tissue. These cell culture models are relatively easy to manufacture, can be produced on demand, are commercially available, have been extensively validated against human tissue in terms of cytokeratin profiles, presence of tight junctions, desmosome (cell-cell) and hemi-desmosome (cell–basement membrane) interfaces, and a basement membrane enriched in laminin-332 and collagen IV [22, 50-52]. The use of immortalised buccal keratinocytes provides further experimental reproducibility than use of primary buccal keratinocytes from individual donors, making these ideal for chemical permeation testing, especially for commercial purposes [22, 24, 52]. Histologically, buccal *in vitro* models form the basal–spinous–superficial stratification typical of *in vivo* buccal epithelium and also display similar chemical permeation profiles to porcine buccal mucosa [53, 54]. The key difference to *in vivo* human buccal mucosa is the strata thicknesses, number of cells, cell-sizes and extracellular space geometries [20]; cell-based *in silico* models can capture these geometric differences directly.

Permeation assays were performed on *in vitro* human buccal mucosa using benzydamine HCl, clobetasol-17-propionate, oxymetazoline HCl and prochlorperazine dimaleate salt, chosen due to either their current use for treatment of oral mucosal conditions or potential use for oral mucosal delivery [23-26]. The permeability was assessed for two *in vitro* models with differing maturity and permeability barrier properties: immature epithelium (immOME; 5 days in culture) and mature epithelium (matOME; 12 days in culture). The advantage of using tissue engineered models here is that they can be manipulated to produce altered biological features that is not possible with animal or human tissue.

Immature mucosa displayed dramatically reduced transcellular and tight junction properties indicating a highly perturbed permeability barrier that allowed chemicals to permeate more readily. Benzydamine, clobetasol propionate and prochlorperazine all interacted with immOME with hyperbolic curve kinetics indicating simple chemical-permeability relationships. In contrast, the permeation profile of oxymetazoline HCl demonstrated sigmoidal-like kinetics, with a slow initial phase followed by rapid permeation from 2 hours, reaching nearly 100% permeation by 5 hours. It could be speculated that this profile may reflect complex chemical-receptor binding within the epithelium on immOME. Oxymetazoline binds with higher affinity to α_{1A}-adrenoreceptors compared to α_{2B}-adrenoreceptors [55]; it is possible that in immOME, increased levels of α_{1A}-adrenoreceptors are present in the epithelium which bind oxymetazoline, retarding its permeation until saturation levels are reached, at which time permeation progresses rapidly. This phenomenon was restricted to immOME as matOME displayed the same permeation profiles for all four chemicals tested. Importantly, the permeation of immature tissue could not be used to predict permeation of mature tissue. By exploiting these differences, we developed three cell-based *in silico* models (one each to mimic immature and mature *in vitro* tissue and one to mimic *in vivo* tissue) allowed for an extrapolation from *in vitro* permeation measurements to *in vivo* predictions.

The immOME was used to capture the impact of passive transport through cell membranes (Q) and matOME to capture the added impact of the buccal mucosal permeability barrier (P_B); this key addition was omitted in our previous work, [20] prohibiting the extrapolation to *in vivo*. The combination of Q and P_B therefore allowed for a mechanistically grounded, chemical-specific prediction of permeation when applied to *in vivo* human tissue geometry.
In all cases, chemical permeation was predicted to be slower *in vivo* than *in vitro* due to the increased epithelial thickness, particularly in the *stratum spinosum* and greater number of keratinocytes. Clobetasol-17-propionate was predicted to permeate fastest, followed by prochlorperazine, benzydamine HCl and oxymetazoline HCl, consistent with differences in passive transport and barrier function. The *in silico* model assumed that the only difference

between mature *in vitro* buccal tissue and *in vivo* buccal tissue is their histological structure, which was directly accounted for.

One of the main advantages of the buccal mucosal delivery route is its high vascularity that provides direct access to the systemic circulation. Studies in rhesus monkeys have shown greater blood flow in the oral mucosa compared to skin [33, 56], which was presumed to be due to increased capillary supply. Our OCTA analysis and that recently published by Zhang *et al*., [57] confirmed this, showing that the buccal mucosa contains a dense vascular network with larger vessel diameters than those found in the skin of the elbow (cubital fossa) or knee (popliteal fossa) [58].

From the capillary network, blood flows via venous drainage into the internal and external jugular veins, enters the heart and is then circulated around the body via the arterial vascular network to other organs. This pathway avoids first pass metabolism, thereby improving bioavailability. A natural extension of the *in silico* permeation model is to include uptake into the vascular system and model whole-body chemical distribution over time as has been performed for other tissues [59-61]. Here, the predicted *in vivo* permeation of oral buccal mucosa was tied to a generic PBPK model for whole-body distribution [16], although there is scope to link our model to more advanced PBPK systems. As PBPK models generally rely on each organ being modelled as a compartment, the tie-in of the cell-based oral mucosa model was achieved by assuming that there was minimal backflow from the lamina propria to the epithelium. In principle, the cell-based model could be coupled directly allowing for backflow, however, this would greatly slow the PBPK computation and, given the relatively large concentration of chemical in the epithelium compared with the blood, is not expected to have a strong impact. The PBPK model showed that whilst, for example, clobetasol-17-propionate was predicted to permeate oral mucosa fastest of the four chemicals tested, the whole-body distribution was more nuanced with a low blood concentration and greater, preferential uptake into lipid-rich tissues and organs like adipose and brain. Such insights highlight the advantage of combining cell-based permeation predictions with PBPK models to provide a more in-depth examination of ADME that is crucial for clinical design and regulatory decision-making, and will expediate drug delivery discovery and up-take for chemicals delivered via the buccal mucosa.

Attempts to validate the oral mucosal-PBPK model are challenging because most *in vivo* data for chemical plasma levels following buccal drug delivery are by 30 second gargle and rinse application, where the chemical has a very short contact time with the oral mucosa, as is the case for benzydamine [62, 63]. These data are not compatible for comparisons with this study where chemicals are placed topically onto the oral mucosa for prolonged periods to mimic

recent advances in mucoadhesive patch technology, where new drug systems are designed for long application times to increase drug uptake [7, 24, 64]. The only appropriate data available that was comparable to this type of delivery was prochlorperazine via an oral mucosal tablet designed to be trapped between the labial and gingival mucosa where it releases chemicals topically to these mucosal tissues. Following further optimised calibration and compensating for drug levels used between the two studies, we found that our oral mucosal-PBPK model successfully predicted systemic exposure following buccal administration of prochlorperazine. Although further refinements are required, the model's ability to accurately predict pharmacokinetic profiles for both intravenous and buccal routes provide confidence in its mechanistic basis. This validation result support the reliability and utility of this modelling framework as a tool for predicting systemic exposure following buccal administration and for comparing intravenous and buccal delivery strategies during pharmaceutical development.

To our knowledge, this study is the first to show predictive *in silico* chemical permeability for *in vivo* human buccal mucosa based on parametrisation of engineered buccal mucosal structure and permeation data. The *in vitro-in silico* extrapolation framework now needs to be extended to include chemicals with more divergent physiochemical properties to produce a larger data set. It also has potential to be developed to biotherapeutic peptides and proteins such as, amongst others, glucagon-like peptide-1 (GLP-1) [65], calcitonin, [66], insulin [67], bradykinin [68], desmopressin [69] or therapeutic-loaded polymeric nanocarriers [70, 71], which have already been tested for delivery via the buccal mucosa.

Although this study reaches new levels of advancements in the *in silico* extrapolation of *in vitro* data to *in vivo* prediction, there are some limitations where further progression can be made. The tissue engineered models in this study used immortalised FNB6 oral keratinocytes that were originally isolated from the healthy buccal mucosa of a female [21]. Although the use of these immortalised keratinocytes allows for experimental standardisation and consistency across chemical testing, they are only representative of a narrow range of the population. Data for permeation of buccal mucosa from both sexes, in a range of ages and ethnicity would be required to improve modelling. Moreover, additional experimental data using chemicals with a wider range of physiochemical properties is required to further parameterise compound-specific effects. Passive transport was modelled while xenobiotic metabolism was not included because the levels of these enzymes within the buccal mucosa is largely unknown. It is possible that these enzyme levels are low, similar to those observed in skin, due to their similar tissue structure and keratinocyte content [72, 73]. Transcriptomic and proteomic studies to profile xenobiotic metabolising enzyme expression and activity are underway on human

buccal mucosa biopsy and tissue engineered buccal models, so that this parameter can be added in a similar manner to those proposed for liver and skin [19, 74].

Extending the *in silico* framework to include intracellular and interstitial fluid protein binding, and presence of efflux transporters (where relevant) would improve predictions for some substrates like the DNA-binding chemical doxorubicin. Additional experimental data on the levels of protein in these intra/extracellular compartments and expression of transporters, specifically for the oral mucosa, is required to further parameterise the *in silico* model.

The current framework also uses 2D cell- based geometry, whereas 3D reconstructions would capture out- of- plane tortuosity and lateral heterogeneity, although the computational cost of a such a 3D model would be significant. Perfect sink conditions at the basal boundary were assumed, excluding the effects of mucosal turnover, salivary clearance or surface dissolution processes; adding these layers and boundary fluxes would increase physiological realism. Moreover, the *in silico* model was assumed quasi-steady as permeation was measured on the timeframe of hours whereas epithelial maturation and remodelling occurs dynamically and is on the timescale of days. Despite these limitations, the *in silico* model provides robust predictions and offers a scalable foundation on which additional biological processes such as xenobiotic metabolism, efflux transporters and dynamic tissue turnover can be applied.

5. Conclusions

This study demonstrates a histology- informed, cell- based *in silico* framework that translates *in vitro* data to *in vivo* predictions for oral mucosa permeability and couples these outputs to a PBPK model for whole-body distribution. A key innovation of this work is the use engineered buccal mucosa of differing maturity, enabling a deeper insight into mechanisms of drug permeation through oral mucosa and facilitating *in vitro* to *in vivo* extrapolation. This *in vitro/in silico* framework offers a powerful tool for improving compound screening, optimising buccal formulations and circumventing the need for animal tissues in future oral mucosal permeation studies. The framework establishes a foundation for expanding predictive modelling across a broader range of chemical classes and for enhancing the design and evaluation of next-generation oral mucosal drug delivery systems.

Data availability

Data is available on request.

Code availability

Code is available on request.

Acknowledgements

The authors would like to thank Dr Rob Bolt (Sheffield Teaching Hospitals NHS Foundation Trust) for collection of human tissue and Prof Ali Khurram (University of Sheffield) for sourcing archival paraffin-wax embedded human oral mucosal tissue. This work was supported by the National Centre for the Replacement, Reduction and Refinement of Animals in Research (NC3Rs) UK, [grant number NC/ W001160-1].

CRediT author statement: SME, ALH, JAL, SDW, HEC, CM and RNB conceptualised research and designed methodology; SME, ALH and JAL performed investigative research, validation and formal data analysis; SME designed, implemented and tested computer code; CM, RNB and HEC secured funding and supervised the project; CM had overall responsibility for project administration; SME, ALH, CM and JAL prepared the draft writing of the manuscript; all authors reviewed and edited the manuscript.

Competing Interest Statement: The authors declare the following financial interests/personal relationships which may be considered as potential competing interests: Craig Murdoch reports that financial support, article publishing charges, and travel were provided by National Centre for the Replacement Refinement and Reduction of Animals in Research. SDW and JAL report a relationship with Syngenta that includes: employment. Other authors declare that they have no known competing financial interests or personal relationships that could have appeared to influence the work reported in this paper.

References

[1] E. Proksch, J.M. Brandner, J.M. Jensen, The skin: an indispensable barrier, Exp Dermatol, 17 (2008) 1063-1072.

[2] T. Otani, M. Furuse, Tight Junction Structure and Function Revisited, Trends Cell Biol, 30 (2020) 805-817.

[3] J. Liu, J. Sun, J. Hu, H. Xue, L. Lei, X. Pan, Biomaterial-based drug delivery strategies for oral mucosa, Colloids Surf B Biointerfaces, 251 (2025) 114604.

[4] S. Malhotra, T. Lijnse, E.O. Cearbhaill, D.J. Brayden, Devices to overcome the buccal mucosal barrier to administer therapeutic peptides, Adv Drug Deliv Rev, 220 (2025) 115572.

[5] J.G. Edmans, K.H. Clitherow, C. Murdoch, P.V. Hatton, S.G. Spain, H.E. Colley, Mucoadhesive Electrospun Fibre-Based Technologies for Oral Medicine, Pharmaceutics, 12 (2020).

[6] S. Bahraminejad, H. Almoazen, Sublingual and Buccal Delivery: A Historical and Scientific Prescriptive, Pharmaceutics, 17 (2025).

[7] M.E. Mauceri, M. Coppini, V. De Caro, G. Di Prima, R. Mauceri, V. Panzarella, G. Giuliana, G. Campisi, Mucoadhesive Drug Delivery Systems for Oral Chronic Inflammatory Mucosal Diseases. The Future is Already Present. A Systematic Review, Oral Dis, (2025).

[8] W.R. Galey, H.K. Lonsdale, S. Nacht, The in vitro permeability of skin and buccal mucosa to selected drugs and tritiated water, J Invest Dermatol, 67 (1976) 713-717.

[9] K. Hashimoto, R.J. DiBella, G. Shklar, Electron microscopic studies of the normal human buccal mucosa, J Invest Dermatol, 47 (1966) 512-525.

[10] H. Zhang, J. Zhang, J.B. Streisand, Oral mucosal drug delivery: clinical pharmacokinetics and therapeutic applications, Clin Pharmacokinet, 41 (2002) 661-680.

[11] M. Samiei, E. Ahmadian, A. Eftekhari, M.A. Eghbal, F. Rezaie, M. Vinken, Cell junctions and oral health, EXCLI J, 18 (2019) 317-330.

[12] B. Xia, Yang, Z., Zhou, H., Lukacova, V., Zhu, W., Milewski, M., Kesisoglou, F., Development of a novel oral cavity compartmental absorption and transit model for sublingual administration: Illustration with zolpidem, AAPS Journal, 13 (2015) 631-642.

[13] S. Polak, C. Ghobadi, H. Mishra, M. Ahamadi, N. Patel, M. Jamei, A. Rostami-Hodjegan, Prediction of concentration-time profile and its inter-individual variability following the dermal drug absorption, J Pharm Sci, 101 (2012) 2584-2595.

[14] J. Kruse, D. Golden, S. Wilkinson, F. Williams, S. Kezic, J. Corish, Analysis, interpretation, and extrapolation of dermal permeation data using diffusion-based mathematical models, J Pharm Sci, 96 (2007) 682-703.

[15] N. Verma, Galula, K., Gupta, R., Rai, B., Multiscale modeling of molecule transport through skin's deeper layers, Computational Toxicology, (2023).

[16] S.A. Peters, Evaluation of a generic physiologically based pharmacokinetic model for lineshape analysis, Clin Pharmacokinet, 47 (2008) 261-275.

[17] A.A. Biswas, M.R. Dhondale, M. Singh, A.K. Agrawal, P. Muthudoss, B. Mishra, D. Kumar, Development and comparison of machine learning models for in-vitro drug permeation prediction from microneedle patch, Eur J Pharm Biopharm, 199 (2024) 114311.

[18] Y. Sun, Brown, M.B., Prapopolou, M., Davey, N., Adams, R.G., Moss, G.P., The application of stochastic machine learning methods in the prediction of skin penetration, Applied Soft Computing, 11 (2011) 2367-2375.

[19] J.A. Leedale, J.A. Kyffin, A.L. Harding, H.E. Colley, C. Murdoch, P. Sharma, D.P. Williams, S.D. Webb, R.N. Bearon, Multiscale modelling of drug transport and metabolism in liver spheroids, Interface Focus, 10 (2020) 20190041.

[20] S.M. Edwards, A.L. Harding, J.A. Leedale, S.D. Webb, H.E. Colley, C. Murdoch, R.N. Bearon, An advanced in silico model of the oral mucosa reveals the impact of extracellular spaces on chemical permeation, Int J Pharm, 666 (2024) 124827.

[21] F. McGregor, E. Wagner, D. Felix, D. Soutar, K. Parkinson, P.R. Harrison, Inappropriate retinoic acid receptor-beta expression in oral dysplasias: correlation with acquisition of the immortal phenotype, Cancer Res, 57 (1997) 3886-3889.

[22] L.R. Jennings, H.E. Colley, J. Ong, F. Panagakos, J.G. Masters, H.M. Trivedi, C. Murdoch, S. Whawell, Development and Characterization of In Vitro Human Oral Mucosal Equivalents Derived from Immortalized Oral Keratinocytes, Tissue Eng Part C Methods, 22 (2016) 1108-1117.

[23] R.S. Turnbull, Benzydamine Hydrochloride (Tantum) in the management of oral inflammatory conditions, J Can Dent Assoc, 61 (1995) 127-134.

[24] H.E. Colley, Z. Said, M.E. Santocildes-Romero, S.R. Baker, K. D'Apice, J. Hansen, L.S. Madsen, M.H. Thornhill, P.V. Hatton, C. Murdoch, Pre-clinical evaluation of novel mucoadhesive bilayer patches for local delivery of clobetasol-17-propionate to the oral mucosa, Biomaterials, 178 (2018) 134-146.

[25] P.G. Hessell, Lloyd-Jones, J.G., Muir, N.C., Parr, G.D., Sugden, K., A comparison of the availability of prochlorperazine following i.m. buccal and oral administration, Int J Pharm, 52 (1989) 159-164.

[26] Y.Z. Feng, X.H. Zeng, The retractive effects of different gingival retraction agents, Hua Xi Kou Qiang Yi Xue Za Zhi, 29 (2011) 53-56.

[27] R.A. Byers, M. Fisher, N.J. Brown, G.M. Tozer, S.J. Matcher, Vascular patterning of subcutaneous mouse fibrosarcomas expressing individual VEGF isoforms can be differentiated using angiographic optical coherence tomography, Biomed Opt Express, 8 (2017) 4551-4567.

[28] M.J. Ju, M. Heisler, A. Athwal, M.V. Sarunic, Y. Jian, Effective bidirectional scanning pattern for optical coherence tomography angiography, Biomed Opt Express, 9 (2018) 2336-2350.

[29] C.C. Miller, The Stokes-Einstein law for diffusion in solution, Proceedings of the Royal Society A, 106 (1924) 724-748.

[30] K. Kwapiszewska, K. Szczepanski, T. Kalwarczyk, B. Michalska, P. Patalas-Krawczyk, J. Szymanski, T. Andryszewski, M. Iwan, J. Duszynski, R. Holyst, Nanoscale Viscosity of Cytoplasm Is Conserved in Human Cell Lines, J Phys Chem Lett, 11 (2020) 6914-6920.

[31] D.I.S. Amestoy. P. R., L'Excellent J-Y., Koster J., A fully asynchronous multifrontal solver using distributed dynamic scheduling, SIAM Journal on Matrix Analysis and Applications, 23 (2001) 1095-7162.

[32] S.G.W. Balay, McInnes, L., Smith, B., Efficient management of parallelism in object oriented numerical software libraries, Birkhäuser, Boston, MA, 1997.

[33] C.A. Squier, D. Nanny, Measurement of blood flow in the oral mucosa and skin of the rhesus monkey using radiolabelled microspheres, Arch Oral Biol, 30 (1985) 313-318.

[34] L.M. Collins, C. Dawes, The surface area of the adult human mouth and thickness of the salivary film covering the teeth and oral mucosa, J Dent Res, 66 (1987) 1300-1302.

[35] K. Mansouri, C.M. Grulke, R.S. Judson, A.J. Williams, OPERA models for predicting physicochemical properties and environmental fate endpoints, J Cheminform, 10 (2018) 10.

[36] T. Rodgers, M. Rowland, Physiologically based pharmacokinetic modelling 2: predicting the tissue distribution of acids, very weak bases, neutrals and zwitterions, J Pharm Sci, 95 (2006) 1238-1257.

[37] B. Gumbiner, K. Simons, A functional assay for proteins involved in establishing an epithelial occluding barrier: identification of a uvomorulin-like polypeptide, J Cell Biol, 102 (1986) 457-468.

[38] B. Srinivasan, A.R. Kolli, M.B. Esch, H.E. Abaci, M.L. Shuler, J.J. Hickman, TEER measurement techniques for in vitro barrier model systems, J Lab Autom, 20 (2015) 107-126.

[39] C.A. Ellison, K.O. Tankersley, C.M. Obringer, G.J. Carr, J. Manwaring, H. Rothe, H. Duplan, C. Genies, S. Gregoire, N.J. Hewitt, C.J. Jamin, M. Klaric, D. Lange, A. Rolaki, A. Schepky, Partition coefficient and diffusion coefficient determinations of 50 compounds in human intact skin, isolated skin layers and isolated stratum corneum lipids, Toxicol In Vitro, 69 (2020) 104990.

[40] T. Rodgers, D. Leahy, M. Rowland, Physiologically based pharmacokinetic modeling 1: predicting the tissue distribution of moderate-to-strong bases, J Pharm Sci, 94 (2005) 1259-1276.

[41] A.O. Isah, M.D. Rawlins, D.N. Bateman, Clinical pharmacology of prochlorperazine in healthy young males, Br J Clin Pharmacol, 32 (1991) 677-684.

[42] W.B. Taylor, D.N. Bateman, Preliminary studies of the pharmacokinetics and pharmacodynamics of prochlorperazine in healthy volunteers, Br J Clin Pharmacol, 23 (1987) 137-142.

[43] A. Finn, J. Collins, R. Voyksner, C. Lindley, Bioavailability and metabolism of prochlorperazine administered via the buccal and oral delivery route, J Clin Pharmacol, 45 (2005) 1383-1390.

[44] FDA. Administration, Roadmap to reducing animal testing in preclinical safety studies, in: fda.gov, 2025.

[45] Y. Huh, D.E. Smith, M.R. Feng, Interspecies scaling and prediction of human clearance: comparison of small- and macro-molecule drugs, Xenobiotica, 41 (2011) 972-987.
[46] S. Catozzi, R. Hill, X.M. Li, S. Dulong, E. Collard, A. Ballesta, Interspecies and in vitro-in vivo scaling for quantitative modeling of whole-body drug pharmacokinetics in patients: Application to the anticancer drug oxaliplatin, CPT Pharmacometrics Syst Pharmacol, 12 (2023) 221-235.
[47] M. Sattar, O.M. Sayed, M.E. Lane, Oral transmucosal drug delivery--current status and future prospects, Int J Pharm, 471 (2014) 498-506.
[48] G. Sa, X. Xiong, T. Wu, J. Yang, S. He, Y. Zhao, Histological features of oral epithelium in seven animal species: As a reference for selecting animal models, Eur J Pharm Sci, 81 (2016) 10-17.
[49] U. Kulkarni, R. Mahalingam, I. Pather, X. Li, B. Jasti, Porcine buccal mucosa as in vitro model: effect of biological and experimental variables, J Pharm Sci, 99 (2010) 1265-1277.
[50] J.K. Buskermolen, C.M. Reijnders, S.W. Spiekstra, T. Steinberg, C.J. Kleverlaan, A.J. Feilzer, A.D. Bakker, S. Gibbs, Development of a Full-Thickness Human Gingiva Equivalent Constructed from Immortalized Keratinocytes and Fibroblasts, Tissue Eng Part C Methods, 22 (2016) 781-791.
[51] S. Gibbs, M. Ponec, Intrinsic regulation of differentiation markers in human epidermis, hard palate and buccal mucosa, Arch Oral Biol, 45 (2000) 149-158.
[52] Z. Said, C. Murdoch, J. Hansen, L. Siim Madsen, H.E. Colley, Corticosteroid delivery using oral mucosa equivalents for the treatment of inflammatory mucosal diseases, Eur J Oral Sci, 129 (2021) e12761.
[53] J. Boateng, O. Okeke, Evaluation of Clay-Functionalized Wafers and Films for Nicotine Replacement Therapy via Buccal Mucosa, Pharmaceutics, 11 (2019).
[54] V. De Caro, G. Giandalia, M.G. Siragusa, C. Paderni, G. Campisi, L.I. Giannola, Evaluation of galantamine transbuccal absorption by reconstituted human oral epithelium and porcine tissue as buccal mucosa models: part I, Eur J Pharm Biopharm, 70 (2008) 869-873.
[55] B. Haenisch, J. Walstab, S. Herberhold, F. Bootz, M. Tschaikin, R. Ramseger, H. Bonisch, Alpha-adrenoceptor agonistic activity of oxymetazoline and xylometazoline, Fundam Clin Pharmacol, 24 (2010) 729-739.
[56] J.W. Canady, G.K. Johnson, C.A. Squier, Measurement of blood flow in the skin and oral mucosa of the rhesus monkey (Macaca mulatta) using laser Doppler flowmetry, Comp Biochem Physiol Comp Physiol, 106 (1993) 61-63.
[57] T. Zhang, Y. Zhang, J. Liao, S. Shepherd, Z. Huang, M. Macluskey, C. Li, Quantitative assessment of the oral microvasculature using optical coherence tomography angiography, Front Bioeng Biotechnol, 12 (2024) 1464562.

[58] R.A. Byers, R. Maiti, S.G. Danby, E.J. Pang, B. Mitchell, M.J. Carre, R. Lewis, M.J. Cork, S.J. Matcher, Sub-clinical assessment of atopic dermatitis severity using angiographic optical coherence tomography, Biomed Opt Express, 9 (2018) 2001-2017.

[59] N. Isoherranen, Physiologically based pharmacokinetic modeling of small molecules: How much progress have we made?, Drug Metab Dispos, 53 (2025) 100013.

[60] J. Leedale, K.J. Sharkey, H.E. Colley, A.M. Norton, D. Peeney, C.L. Mason, J.G. Sathish, C. Murdoch, P. Sharma, S.D. Webb, A Combined In Vitro/In Silico Approach to Identifying Off-Target Receptor Toxicity, iScience, 4 (2018) 84-96.

[61] W.A. Murphy, J. Adiwidjaja, N. Sjostedt, K. Yang, J.J. Beaudoin, J. Spires, S.Q. Siler, S. Neuhoff, K.L.R. Brouwer, Considerations for Physiologically Based Modeling in Liver Disease: From Nonalcoholic Fatty Liver (NAFL) to Nonalcoholic Steatohepatitis (NASH), Clin Pharmacol Ther, 113 (2023) 275-297.

[62] G.A. Baldock, R.R. Brodie, L.F. Chasseaud, T. Taylor, L.M. Walmsley, B. Catanese, Pharmacokinetics of benzydamine after intravenous, oral, and topical doses to human subjects, Biopharm Drug Dispos, 12 (1991) 481-492.

[63] L.F. Chasseaud, B. Catanese, Pharmacokinetics of benzydamine, Int J Tissue React, 7 (1985) 195-204.

[64] S. Jacob, A.B. Nair, S.H.S. Boddu, B. Gorain, N. Sreeharsha, J. Shah, An Updated Overview of the Emerging Role of Patch and Film-Based Buccal Delivery Systems, Pharmaceutics, 13 (2021).

[65] M.K. Gutniak, H. Larsson, S.J. Heiber, O.T. Juneskans, J.J. Holst, B. Ahren, Potential therapeutic levels of glucagon-like peptide I achieved in humans by a buccal tablet, Diabetes Care, 19 (1996) 843-848.

[66] T. Caon, L. Jin, C.M. Simoes, R.S. Norton, J.A. Nicolazzo, Enhancing the buccal mucosal delivery of peptide and protein therapeutics, Pharm Res, 32 (2015) 1-21.

[67] M.G. Lancina, 3rd, R.K. Shankar, H. Yang, Chitosan nanofibers for transbuccal insulin delivery, J Biomed Mater Res A, 105 (2017) 1252-1259.

[68] J.G. Edmans, C. Murdoch, P.V. Hatton, L.S. Madsen, M.E. Santocildes-Romero, S.G. Spain, H.E. Colley, Bioactive Protein and Peptide Release from a Mucoadhesive Electrospun Membrane, Biomed Mater Devices, 2 (2024) 444-453.

[69] M.B. Stie, J.R. Gatke, I.S. Chronakis, J. Jacobsen, H.M. Nielsen, Mucoadhesive Electrospun Nanofiber-Based Hybrid System with Controlled and Unidirectional Release of Desmopressin, Int J Mol Sci, 23 (2022).

[70] V. Hearnden, H. Lomas, S. Macneil, M. Thornhill, C. Murdoch, A. Lewis, J. Madsen, A. Blanazs, S. Armes, G. Battaglia, Diffusion studies of nanometer polymersomes across tissue engineered human oral mucosa, Pharm Res, 26 (2009) 1718-1728.

[71] J.G. Edmans, S. Harrison, P.V. Hatton, C. Murdoch, S.G. Spain, H.E. Colley, Electrospinning polymersomes into bead-on-string polyethylene oxide fibres for the delivery of biopharmaceuticals to mucosal epithelia, Biomater Adv, 157 (2024) 213734.

[72] S.A. Smith, H.E. Colley, P. Sharma, K.M. Slowik, R. Sison-Young, A. Sneddon, S.D. Webb, C. Murdoch, Expression and enzyme activity of cytochrome P450 enzymes CYP3A4 and CYP3A5 in human skin and tissue-engineered skin equivalents, Exp Dermatol, 27 (2018) 473-475.

[73] S. Kazem, E.C. Linssen, S. Gibbs, Skin metabolism phase I and phase II enzymes in native and reconstructed human skin: a short review, Drug Discov Today, 24 (2019) 1899-1910.

[74] J.J. Madden, Webb, S.D., Enoch, S.J., Colley, H.C., Murdoch, C., Shipley, R., Sharma, P., Yang, C., Cronin, M.T.D., In silico prediction of skin metabolism and its implication in toxicity assessment, Computational Toxicology, 3 (2017) 44-57.